

Experimental and Theoretical Electron Density Studies in Large Molecules: NAD⁺, β -Nicotinamide Adenine Dinucleotide

Benoît Guillot,[†] Nicolas Muzet,[†] Emilio Artacho,[‡] Claude Lecomte,[†] and Christian Jelsch^{*,†}

Laboratoire de Cristallographie et Modélisation des Matériaux Minéraux et Biologiques (LCM3B), CNRS UMR 7036, Université H. Poincaré, Vandoeuvre-les-Nancy, France, and Department of Earth Sciences, University of Cambridge, Downing Street, Cambridge CB2 3EQ, U.K.

Received: February 25, 2003; In Final Form: May 27, 2003

NAD⁺ is the oxidized form of the coenzyme redox pair NAD⁺/NADH and plays a main role in catalysis of biological processes. Accurate X-ray diffraction data have been collected at 100 K from a crystal of the free acid form of the coenzyme NAD⁺ with a CCD area detector up to 0.55 Å resolution. A multipole refinement was carried out, and the electron density of the molecule has been analyzed in order to further model its interaction with enzymes. The electron density of NAD⁺ has also been computed by a DFT (density functional theory) approach. The charge density and electrostatic potential obtained from experiment and theory compare well. There is a very good agreement between the theoretical and experimental charge densities for all the C–C and C–N type connections of the NAD⁺ molecule; this is less the case for the pyrophosphate region. The experimental electron density lone pairs of the pyrophosphate lateral oxygen atoms are distorted by hydrogen bonds effects. The electrostatic potential has large spatial extensions with highly positive and negative regions, suggesting that NAD⁺ is likely to interact with proteins mostly by electrostatic interactions.

Introduction

Nicotinamide adenine dinucleotide cofactor (NAD⁺) plays a major role in enzyme-catalyzed biological oxido-reduction processes. NAD⁺ is the oxidized form of the redox pair NAD⁺/NADH and binds to enzymes involved in metabolic oxidation reactions, mostly dehydrogenase reactions. NAD⁺ is composed of a pyrophosphate moiety linking together an adenylic acid and a nicotinamide-5'-ribonucleotide group. In the dehydrogenation process, NAD⁺ is reduced to NADH by accepting an hydride anion (H[−]) from the substrate to its redox active site located on the C18 atom (in the present paper nomenclature) of the nicotinamide ring. When the cofactor has formed a reactive complex with an enzyme, the carboxamide group loses freedom of rotation, owing to intermolecular binding forces such as hydrogen bonds.

The ubiquitous redox cofactors nicotinamide adenine dinucleotides [NAD⁺/NADP⁺] are very similar molecules, despite their participation in substantially different biochemical processes. NADP⁺ differs from NAD⁺ only by the presence of an additional phosphate group esterified to a hydroxyl group of the adenine side ribose. NADP⁺ is confined with few exceptions to the reactions of reductive biosynthesis, whereas NAD⁺ is used almost exclusively in oxidative degradations.

There are many known tertiary structures of NADP⁺ and NAD⁺ protein complexes. The conserved and variable interactions between the two cofactors and their respective binding pockets in several proteins are reported in detail in the reviews of Carugo et al.^{1,2} A clear fingerprint in NAD⁺ complexes is a carboxylate side chain that chelates the diol group at the ribose near the adenine, whereas in NADP⁺ complexes an arginine

side chain faces the adenine plane and interacts with the phosphomonoester moiety. The NADP⁺ coenzymes are more flexible in conformation than those of NAD⁺. The protein cofactor interactions are largely conserved in the NAD⁺ complexes, while they are quite variable in those of NADP⁺. In both cases the pocket around the nicotinamide moiety is substrate dependent and rules the stereospecificity of the chemical process involving the cofactor.

Experimental and theoretical studies on model compounds for such a reaction have suggested that the favored mechanism involves hydride transfer to the face of the NADH pyridine ring near the carbonyl oxygen.³ On the basis of the quantum chemical energy calculations of the transition state by Donkersloot and Buck,⁴ it has been suggested that the stereospecific property of the reaction is induced by an interaction between the negatively charged carboxamide oxygen atom and the positive charge of the hydride donating moiety.

A distortion of the nicotinamide ring of NADH was observed in the 1 Å resolution crystal structure of horse liver alcohol dehydrogenase in complex with NADH.⁵ Quantum chemical calculations showed that the puckering of the pyridine ring activates NADH for enzymatic hydride transfer.

Information on the relationship between the electronic properties and molecular conformations of NAD⁺ will enable understanding the electron and hydride transfer in biological processes and the reaction mechanism of dehydrogenase and hydrogenase processes at the electronic level. Therefore, the aim of this study is a description of the charge density and electrostatic properties of the NAD⁺ molecule.

The accurate crystal structure of the nicotinamide molecule was determined from X-ray and neutron diffraction experiments by Miwa et al.⁶ An estimation of the electron distribution by the maximum entropy method indicates that the electrostatic properties depend on the rotation of the carboxamide group out of the pyridine plane. But, to the best of our knowledge, no

* To whom correspondence should be addressed. E-mail: jelsch@lcm3b.uhp-nancy.fr.

[†] Université H. Poincaré.

[‡] University of Cambridge.

detailed ab initio calculation or experimental determination of the charge density of NAD^+ has been undertaken. Some theoretical calculations were performed for calculating atomic point charges to be used in force field parametrization,⁷ based on geometrical optimization comparison. Therefore, to accurately determine the electrostatic properties of NAD^+ , DFT calculations and experimental high-resolution X-ray diffraction analyses ($X - (X + N)$)⁸ have been performed. Such a theoretical calculation on a large molecule like NAD^+ and the resulting properties have to be calibrated against the experimental charge density study. This comparison will also determine the minimal basis sets required to accurately analyze the interaction of NAD^+/NADH with proteins in further calculations.⁹

The experimental charge density determination of this molecule of 48 non-hydrogen atoms, crystallizing in the $P1$ space group, requires neutron diffraction data to determine accurate hydrogen atoms positional and anisotropic thermal motion displacement parameters (ADPs). The high-resolution neutron crystal structure of NAD^+ has therefore been recently determined.¹⁰

Finally, another aim of the present crystallographic analysis is to expand our database of multipolar parameters¹¹ describing the electron density of biological molecules, including proteins and nucleic acids. This database is the starting point for electrostatic experimental force field parameters. Furthermore, the resulting charge density parameters are presently being used in the multipolar refinement of the ultrahigh resolution aldose reductase–inhibitor– NAD^+ complex.⁹

Experimental Section

X-ray Data Collection. NAD^+ was purchased from SIGMA (St Louis, MO). In the present study, NAD^+ differs from that under physiological conditions, as its adenine base is protonated. The conditions yielding triclinic crystals of the acidic form of NAD^+ in an aqueous solution of 50% methanol were already described.¹² The Mo $K\alpha$ X-ray diffraction intensities were measured with a Nonius Kappa CCD diffractometer at 100 K using a nitrogen vapor open flow stream device (Oxford Cryosystems cooler 600 series). The data collection strategy was performed with the programs COLLECT and STRATEGY.¹³ The maximum 2θ swing angle was 35° ($\sin \theta_{\max}/\lambda = 0.91 \text{ \AA}^{-1}$, $d_{\min} = 0.55 \text{ \AA}$), and the crystal-to-detector distance was fixed to 50 mm. A total of 4565 frames was collected over a 6 day period.

The intensity integration was performed using DENZO.¹⁴ The final unit cell parameters were refined with the SCALEPACK¹⁴ program using all the frames. More experimental details and intensity statistics are summarized in Table 1. The diffraction frames scaling was performed using the SCALEPACK program. The Friedel pairs were merged during the scaling procedure. As NAD^+ crystallizes in the $P1$ space group, much attention was paid to ensure high redundancy: the final redundancy depends on the resolution, varying continuously from 17 to about 2, respectively, for the lowest and highest resolution shells. The signal to noise ratio is very high, with an average $I/\sigma(I)$ value of 32, and less than 2% of the averaged data present a $I/\sigma(I)$ ratio less than 3.

Electron Density Models and Refinement Strategy. The initial non-hydrogen atoms' coordinates were taken from the neutron structure of NAD^+ .¹⁰ The atomic numbering is shown in Figure 1. All hydrogen atoms were clearly located in the X-ray difference Fourier maps, demonstrating the diffraction data quality. The least-squares refinement program MoPro¹⁵ was used to refine the structure and charge density of NAD^+ . The

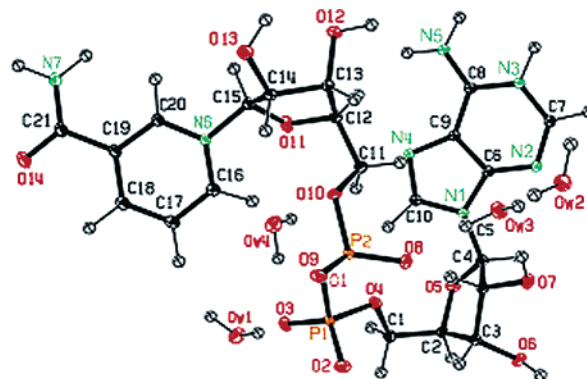


Figure 1. ORTEP view⁴⁵ of the NAD^+ molecule. Displacement ellipsoids are shown at the 50% probability level. The NAD^+ molecule studied here is a formally neutral bis-zwitterion, with N6 and N3–H formally positive, and O3–P1–O2 and O1–P2–O8 formally negative.

TABLE 1: Summary of Experimental Conditions and X-ray Crystallographic Diffraction Data

formula	$\text{C}_{21}\text{H}_{27}\text{N}_7\text{O}_{14}\text{P}_2 + 4\text{H}_2\text{O}$
space group	triclinic $P1$
temperature (K)	100(5)
a b c (Å)	8.592(10) 8.845(10) 11.192(10)
α β γ (deg)	109.64(5) 90.56(5) 103.92(5)
V (Å ³)	773.71
Z F(0 0 0)	1 384e
density calc (g/cm ³)	1.578
crystal size	$0.35 \times 0.35 \times 0.30 \text{ mm}^3$
radiation type	Mo $K\alpha$
wavelength λ (Å)	0.7107
monochromator	graphite
scan width $\Delta\omega$ (deg)	0.5–1
time per step min/max. (s)	150–300
max. $\sin \theta/\lambda$ (Å ^{−1})	0.91 (0.55 Å)
redundancy	16.0
completeness (%)	88.4
$wR(I)$ merge (%)	2.3
N measured	154 769
N unique	9643 9504 ($I > 3\sigma$)

TABLE 2: Summary of Conventional and Multipolar Refinements^a

	spherical atom model		multipolar refinement	
	$ F /\sigma(F) > 0$	$ F > 3\sigma(F)$	$ F /\sigma(F) > 0$	$ F > 3\sigma(F)$
nb. of observations	9617	9504	9617	9504
$R(F)$ (%)	2.33	2.24	1.26	1.22
$wR(F)$ (%)	3.28	3.12	1.25	1.24
goodness of fit	2.83	2.75	1.08	1.08

^a $wR(F) = [\sum w(F_o - kF_c)^2 / \sum wF_o^2]^{1/2}$. $R(F) = \sum (F_o - kF_c) / \sum F_o$. $\text{gof} = [\sum w(F_o - kF_c)^2 / (N_{\text{obs}} - N_{\text{var}})]^{1/2}$. Weighting scheme: $w = 1/\sigma^2(F)$.

least squares refinement was performed against the 9504 structure factor moduli with $|F_H| > 3\sigma(|F_H|)$. As the origin is undetermined in the space group $P1$, the position of the O1 atom was kept fixed during all the refinements.

Spherical Atom Refinement. First, positional and anisotropic displacement parameters (ADPs) of the non-hydrogen atoms were refined against the high order reflections ($\sin \theta/\lambda > 0.8 \text{ \AA}^{-1}$). This was followed by a refinement of the same parameters for the H atoms using low-order data ($\sin \theta/\lambda < 0.5 \text{ \AA}^{-1}$). This procedure was iterated until convergence. The scale factor was refined at the beginning of each refinement step. The crystallographic residual at the end of the spherical atom refinement is given in Table 2.

To transfer positional and thermal parameters of the H atoms from the neutron structure,¹⁰ the isotropic thermal displacement parameters of the non-hydrogen atoms derived from X-ray and

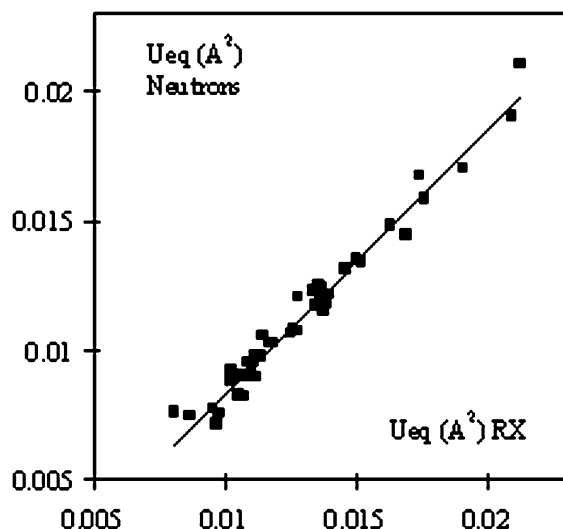


Figure 2. Plot of the isotropic thermal displacement parameters of non-hydrogen atoms of the neutron structure against those of the X-ray structure.

neutron data were compared, as shown in Figure 2. The neutron ADPs had to be linearly scaled to the X-ray parameters using the following relationship:

$$U_{rx} = 1.16(9)U_n$$

Such a scaling is partly related to the difference between the X-ray and neutron¹⁰ experiment temperatures, as confirmed by the cell parameters' differences (Table 1). Another explanation could be the lack of monochromaticity of the Mo X-ray beam operated at 50 kV with a graphite monochromator, as shown recently by Lenstra et al.¹⁶ These authors studied the systematic errors in the ADPs determined from a Mo tube operated at a 50 kV acceleration voltage with a graphite monochromator, which yields a significantly nonmonochromatic beam. Therefore, the hydrogen atoms' ADPs, obtained from the neutron experiment, were corrected for the proportionality coefficient and were subsequently kept fixed during the refinement.

Multipolar Refinement. The atomic electron density was modeled with the program MoPro,¹⁵ as the sum of the core-plus-valence spherical electron density, and the nonspherical valence density was described as a sum of multipoles:¹⁷

$$\rho(\vec{r}) = \rho_{\text{core}}(r) + P_{\text{val}}\kappa^3\rho_{\text{val}}(\kappa r) + \sum_{l=0}^{l_{\text{max}}} \kappa'^3 R_{n_l}(\kappa' r) \sum_{m=0}^l P_{lm} \mp y_{lm\pm}(\theta, \varphi) \quad (1)$$

P_{val} is the valence population parameter and gives an estimation of the net atomic charge $q = N_{\text{val}} - P_{\text{val}}$, where N_{val} is the number of valence electrons. $y_{lm\pm}$ represent multipolar spherical harmonic functions of order l in real form, R_{nl} are Slater type radial functions, and $P_{lm\pm}$ are the multipolar populations. The coefficients κ and κ' describe the contraction–expansion for the spherical and multipolar valence densities, respectively. For the structure factor computations, the form factor for the hydrogen atoms was taken from Stewart et al.,¹⁸ the form factors for non-hydrogen atoms were calculated from Clementi and Raimondi¹⁹ wave functions, and the real and imaginary dispersion corrections to the form factors were from Cromer.²⁰

The multipole expansion was truncated at the hexadecapole level for P, and at the octapole level for O, N, and C atoms. The pyrophosphate oxygen atoms were given specific Slater

TABLE 3: Coefficients of the Radial Slater Functions Used for the Multipoles Definition (Dipole, Quadrupole, Octapole, Hexadecapole) of the Different Atoms

atom	ζ (bohr ⁻¹)	n_1	n_2	n_3	n_4
P	3.60	6	6	6	6
N	3.80	2	2	3	
C	3.00	2	2	3	
H	2.26	1	2		
O (C–O–X)	4.50	1	2	4	
O (P–O–P)	3.50	1	2	4	
O (O=P)	4.50	2	2	3	

functions⁸ (Table 3). For hydrogen atoms, all dipoles and quadrupoles were refined. Local axis systems were chosen in order to be able to apply at the beginning of the refinement process a maximal number of geometrical constraints (e.g. two mirror planes for atoms belonging to aromatic rings). Furthermore, with such an axes definition, a database¹¹ with a reduced number of significant parameters can be built. At the beginning of the charge density refinement, the multipoles were constrained to obey chemical and local symmetry constraints in order to get a good start. A chemical constraint was applied through the twofold pseudosymmetry around the O1 atom to the pyrophosphate and ribose moieties. All the atoms similar on a chemical basis (OH, O⁻, P, H₂O, H_N, H_{Csp²} and H_{Csp³}, C_{sp²} and C_{sp³}, ...) were set to be identical. For the water molecules, only two atom types (H_w and O_w) were defined.

The number of (κ , κ') parameter pairs refined was 38 for all different non-hydrogen atom types. All hydrogen atoms, belonging to the same category H₂O, H_N, H_{Csp²}, and H_{Csp³}, were assigned a unique (κ , κ') pair, except for atoms HN3 and HC7.

Some of the expansion/contraction coefficients of the pyrophosphate group were restrained,¹⁵ as they turned out to refine to unrealistic values, using the following targets and standard deviations: $\kappa(\text{P}) = 1.05 \pm 0.02$, $\kappa'(\text{P}) = 1.04 \pm 0.03$, $\kappa(\text{O}(\text{P})) = 0.969 \pm 0.01$. These target values and standard deviations were taken from the database of charge density parameters.¹¹ These restraints were also necessary to obtain realistic valence populations on these atoms. All these new restraints are straightforward to apply in the new version of MoPro. In the final stages of the refinement, all restraints were removed and the corresponding parameters turned out to remain stable.

As NAD⁺ is among the largest molecule on which a charge density analysis was performed so far, the details of the refinement process deserve description. The charge density parameters were refined in the $0 < s < 0.91 \text{ \AA}^{-1}$ range ($I > \sigma(I)$), using a quite similar strategy to that used for the first charge density refinement of a large molecule:²¹ (a) scale factor; (b) multipoles $P_{lm\pm}$; (c) valence P_{val} and then κ ; (d) $\{P_{lm}$ and $P_{\text{val}}\}$ and G isotropic Gaussian extinction of type 1; (e) $\{xyz, U^{ij}\}$ of C, N, O, P atoms in the $0.8\text{--}0.91 \text{ \AA}^{-1}$ range.

This process was cycled until convergence, while the chemical and symmetry constraints were progressively released. The NAD⁺ and the water molecules were constrained to be electrically neutral. Finally the following refinements were carried out iteratively several times until convergence: (f) scale factor and G ; (g) $\{P_{lm\pm}$ and $P_{\text{val}}\}$; (h) κ' ; (i) $\{P_{lm\pm} xyz, U^{ij}\}$ of C, N, O, P atoms.

In the residual electron density map computed after the final multipolar refinement (with the reflections $\sin \theta/\lambda < 0.8 \text{ \AA}^{-1}$ and $F > 3\sigma_F$), the maximum and minimum density do not exceed $\pm 0.05 \text{ e \AA}^{-3}$. The final crystallographic statistical indices are given in Table 2. Their extremely low values testify for the quality of the data and refinement model. The best fractional coordinates and ADPs from multipolar refinement are published as Supporting Information.

The rigid bond test²² for non-H atoms after the X-ray multipolar refinement displays an average value of $0.4(3) \times 10^{-3} \text{ \AA}^2$, well below 10^{-3} \AA^2 , except for the C2–O5 bond, for which the difference between the mean-square displacement tensors along the bond reaches $1.5 \times 10^{-3} \text{ \AA}^2$. This indicates that ADPs are expected to be reliable and well deconvoluted from the deformation of the electron density. The experimental electrostatic potential was computed with the program ELEC-TROS.²³

The topological analysis of the total electron density ρ allows location of the critical points (CPs) where the gradient is nullified $\nabla\rho(\mathbf{r}) = \mathbf{0}$. The nature of the critical point is determined by analyzing the principal axes (eigenvectors) and curvatures (eigenvalues) of the Hessian matrix $\{\partial^2\rho/\partial x_i\partial x_j\}$. Each CP is characterized by a (ω, σ) pair, where ω is the number of nonzero eigenvalues and σ is the sum of their signs (signature). For example, a $(3, -1)$ bond critical point has three nonzero eigenvalues, two of them being negative and one positive. Generally, an “organic” covalent bond has a $(3, -1)$ CP associated with a large electron density $\rho(r)$ and negative Laplacian $\nabla^2\rho(r)$. On the other hand, ionic and hydrogen bonds have a $(3, -1)$ CP associated with a lower $\rho(r)$ and a positive Laplacian. Another useful quantity is the ellipticity of a bond, defined as $\epsilon = \lambda_1/\lambda_2 - 1$, where λ_1 and λ_2 are the curvatures of the electron density in the plane perpendicular to the bond ($|\lambda_1| \geq |\lambda_2|$). The ellipticity represents the deviation from the cylindrical symmetry for which ϵ is equal to zero. A high λ_3 along a hydrogen bond path is an indicator for strong H bonds.²⁴

The topology of the experimental electron density has been analyzed using the NEWPROP program.²⁵ The average standard uncertainties of the position and of the density at the critical point (CP in the following) are estimated to be about 10^{-3} \AA and 0.05 e \AA^{-3} , respectively. The standard uncertainty on the second derivatives λ_i of the electron density is estimated to be $\sim 10\%$ of their values.²⁴

Theoretical Calculations

All calculations were performed with the DFT method Siesta^{26,27} with the NAD⁺ atomic coordinates fixed at their crystallographic values. This software allows calculations that scale linearly with the atom number in the system (instead of scaling with the cube of the atom number). Some of the approximations made are described in the following, and a detailed description can be found in refs 26 and 28. Exchange and correlation of the Kohn–Sham theory²⁹ are treated with the generalized gradient approximation (GGA) functional proposed by Perdew, Burke, and Ernzerhof.³⁰ Core electrons are replaced by scalar-relativistic norm-conserving pseudopotentials generated using the Troullier–Martins scheme³¹ in their fully nonlocal formulation.³² The following core radii seen by the orbitals, in atomic units, were used: 1.33 for the s, p atomic orbitals of carbon, 1.21 for the s, p orbitals of nitrogen, 1.14 for the s, p orbitals of oxygen, and 1.25 for the s orbitals of hydrogen atoms. A uniform mesh with a plane-wave cutoff of 100 Ry was used to represent the Hartree and exchange-correlation potentials and the local part of the pseudopotential.

Valence electrons were described using a basis set of finite-range numerical atomic orbitals. Radial parts of these orbitals are based on the scheme of pseudoatomic orbitals of Sankey and Niklewski,³³ who proposed a scheme to build single- ζ bases. In Siesta, they are generalized to arbitrarily complete bases up to double- ζ with polarization orbitals.²⁸ The orbital confinement energy shift²⁸ defines a R_c radius for each single- ζ orbital above which this one vanishes. R_c values are different for each atom

TABLE 4: Atomic Orbitals’ Radii R_c in Atomic Units (bohr) for Each l Shell^a

atom	energy shift (meV)	split norm (%)	$l = 0$		$l = 1$	
			$\zeta = 1$	$\zeta = 2$	$\zeta = 1$	$\zeta = 2$
H	13.6	0.50	8.800	2.519		
C	13.6	0.35	5.802	2.810	7.450	2.810
N	10.9	0.35	5.099	2.349	6.547	2.291
O	6.8	0.35	4.809	2.030	6.175	1.955
P	6.8	0.35	6.468	3.335	8.516	3.640

^a ζ stands for each of the split valence orbitals.

and orbital and lie between 5 and 9 (see Table 4). Numerical multiple- ζ bases are built with the split valence.²⁸ Finally, the $l + 1$ orbital is added to polarize the most extended atomic valence orbital (l). The latter is numerically obtained from the polarization of the pseudoatom in the presence of a small electric field.²⁷ The cutoff radius of these orbitals is defined by the range of the orbitals that they polarize. In the present work, we have used a double- ζ basis with one polarization orbital for all atoms.

The final set of cutoff value has been selected so the density compares well to that of calculations done with the lowest energy shift available (1.4 meV) and is the closest possible to the experimental density. The longest cutoffs are needed for the O, N, and P (E_{shift} , respectively, 6.8, 10.9, and 6.8 meV) atoms, while shorter distances are acceptable for C and H (E_{shift} 13.6 meV). Cutoff radii R_c are reported in Table 4. The shape of the deformation density is strongly sensitive to the *split norm* parameter. Indeed, bad choices of these values regularly lead to multiple maxima on the bonding deformation densities. A split norm parameter of 0.35% gives reasonable results. For the H atom, a parameter of 0.50% is needed;²⁸ otherwise, the X–H bonding density rises to an unrealistically high level.

The use of these finite range orbitals, that give rise to sparse overlap and Hamiltonian matrixes, and of pseudopotentials in the Kleinman–Bylander factorized form allows us to build the Kohn–Sham Hamiltonian with order- N operations.²⁷ Siesta works with the valence density within the pseudopotential field. Therefore, the core electron density is not available and no topological analysis of the total density was performed. Calculations were performed in the periodic medium of the triclinic cell.

A “gas phase” calculation was made increasing the box size by centering NAD⁺ in a box which is 10 \AA wider than the experimental one in every direction. As DFT calculations in the gas phase, especially for anionic charge densities, should be taken with caution,^{34,35} we used Gaussian 98³⁶ software to get a set of atomic charges, with the MP2, HF, and B3LYP methods, for comparison purposes. Atoms in these calculations were described by the standard 6-31G* basis set.

Deformation Electron Density and Topology

Nicotinamide Group. The static electron density maps in the nicotinamide base plane show an excellent qualitative and quantitative agreement, as testified by Figure 3. The difference density in the nicotinamide pyridine ring, obtained by algebraic subtraction between theoretical and experimental deformation densities, is also given: experimental and DFT electron density maps agree within 0.1 e/\AA^3 . This agreement also applies to the deformation densities of the X–H bonds. The largest difference appears around atom O14, for which the rigid bond test²³ is not satisfied.

Adenine Base. The agreement between experiment and theory is also excellent for the adenine base: the theoretical and experimental electron densities differ by less than 0.1 e/\AA^3

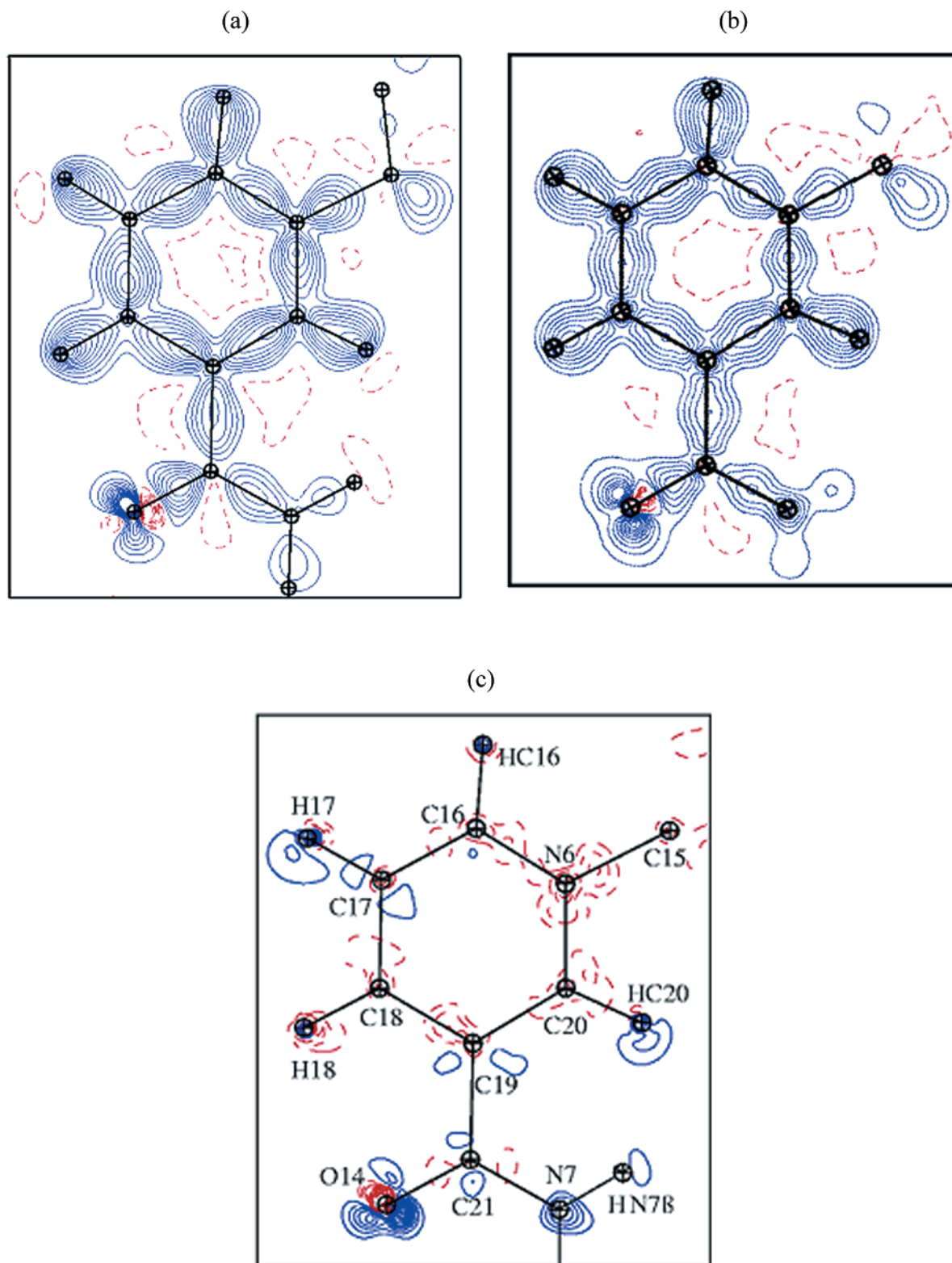


Figure 3. Static deformation electron density in the nicotinamide plane: (a) experimental; (b) theoretical (contour $\pm 0.1 \text{ e}/\text{\AA}^3$); (c) difference of theory - experiment (contour $\pm 0.05 \text{ e}/\text{\AA}^3$; positive, blue; negative, red). Zero omitted.

(Figure 4). The only two exceptions ($\Delta\rho = -0.3 \text{ e}/\text{\AA}^3$) relate to the densities of the C10–HC10 bond and of the N4 nitrogen atom lone pair. Nevertheless, these large discrepancies are systematically located very close to the atom nuclei, where charge density results have a higher uncertainty due to the finite experimental resolution of X-ray data and to the pseudopotentials used in the SIESTA calculations. Discrepancies between theory and experiments similar to those discussed in this paper

were analyzed in a previous study of the peptide bonds in the protein crambin,³⁷ where the effect of the different approximations within the theoretical method was scrutinized. The largest deviations appear, in this study, around the oxygen atoms' lone pairs. Surprisingly, it was found that the deviations are not due to the set of orbitals used as basis but due to either the pseudopotentials or the density functional. The changes between the present PBE GGA and the local density approximation are

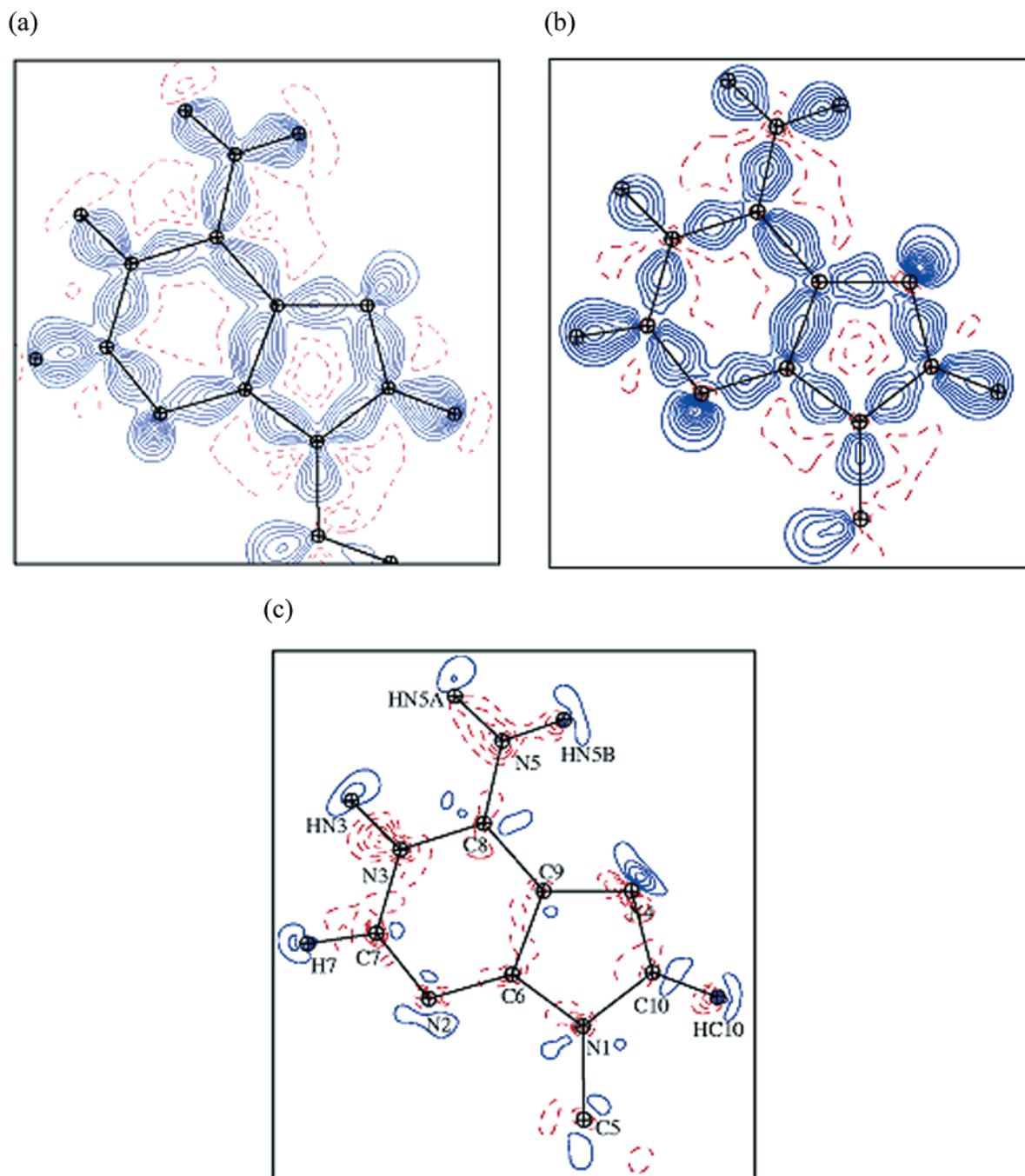


Figure 4. Static deformation electron density in the adenine plane: (a) experimental; (b) theoretical; (c) difference of theory – experiment. Contour as in Figure 3.

however considerably smaller than the discrepancies between theory and experiment. Performing calculations beyond the pseudopotential approximation and density functional theory represents a demanding effort largely unjustified, given the satisfactory accuracy of the present methodology.

The experimental charge density topology of the adenine ring is of great interest, since the protonation of the pyrimidine N3 atom implies several resonating canonical forms (Figure 5). It was shown on the basis of bond lengths in a sample of 13 structures containing a protonated adenine³⁸ that canonical forms 2 and 4 contribute more significantly to the resonance scheme. In the case of an interaction of a trichlorozinc group with the N4 atom of the N3-protonated base, it was observed that form 2 is favored.³⁹ Examination of the C–N interatomic distances allows us to gather them into two categories (Table 5b): C7–N2, C8–N5, and C10–N4 bonds have similar lengths of about

1.32 Å, whereas the remaining C–N bonds are all larger than 1.35 Å. This suggests that the bonds of the first category have a more pronounced double bond character and that canonical form 2 of the N3-protonated adenine base is the most compatible with this observation (Figure 5). The C9–C8 (1.412 Å) and C9–C6 (1.392 Å) bonds have lengths close to that of the C–C bond of benzene (1.397 Å). The comparison of the bond lengths as well as the electron densities and ellipticity values at the CPs (Table 5b) suggests that C6–C9 has a slightly stronger double bond character than C9–C8, indicating a partial preference for structures 1 and 2 over structures 3 and 4 in Figure 5. Therefore, the resonant form 2 is likely to be dominant with the occurrence of other forms. The topological properties fully confirm this hypothesis, since the electron densities at the C7–N2, C8–N5, and C10–N4 bonds' CPs are higher than 2.4 e/Å³, whereas all other C–N bonds of the adenine base have values

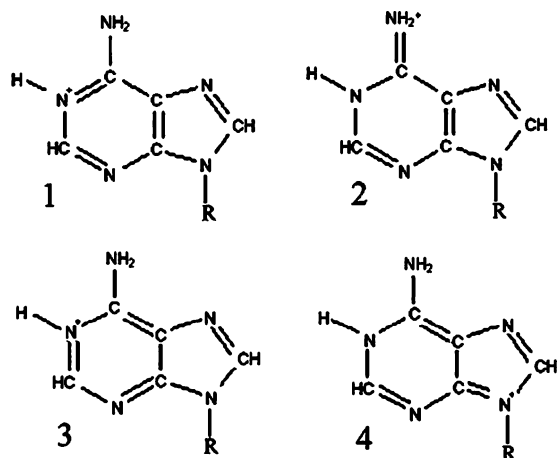


Figure 5. Four possible resonant forms of the N3-protonated adenine.

ranging between 2.1 and 2.2 e/Å³. Furthermore, the experimental and theoretical results agree with previous charge density studies of other molecules containing a protonated adenine:^{39,40} the highest deformation density peaks in the adenine plane are on the C6–C9 and C9–C8 bonds.

Ribose Rings. The experimental and theoretical deformation densities of the two ribose rings agree very well except for the hydroxyl oxygen lone pairs. As mentioned in the NAD⁺ neutron structure study,¹⁰ the C–O bond lengths of the ribose ether groups are split in two groups: C4–O5 ($d = 1.408$ Å), C15–O11 ($d = 1.392$ Å), near the bases, and C12–O11 ($d = 1.451$ Å), C2–O5 ($d = 1.454$ Å), near the pyrophosphate. This correlates well with the large electron density and Laplacian values at the CP ($\rho_{cp} \approx 1.9$ e/Å³ and $\nabla^2\rho \approx -12.5$ e/Å⁵) observed for the C5–O5 and C15–O11 bonds. The C2–O5 and C12–O11 bonds display smaller values: $\rho_{cp} \approx 1.5$ e/Å³ and $\nabla^2\rho \approx -6$ e/Å⁵. The shorter ether bond lengths on the bases' side could be related to the electron withdrawing effect of the N6 and N1 nitrogen atoms of the bases, while the electron withdrawing pyrophosphate oxygen atoms are separated from the ether group by a supplementary carbon atom.

Pyrophosphate Group. The agreement between experiment and DFT calculation is generally poorer in the region of the phosphorus atoms. The peaks of the static deformation density are located at the same position in the experimental and theoretical maps (Figure 6), but the P–O peak heights and oxygen lone pairs' densities are different. There is a pseudodyad axis passing through the middle of the pyrophosphate moiety relating the two nucleotides (Figure 1) if the differences between the two base rings are neglected. However, significant differences are found between the two sides of the molecule, especially for the O1–P bonds. The experimental deformation density (Figure 6) is stronger on the O–P1 bond ($\rho = 0.60$ e/Å³) than on the O–P2 bond ($\rho = 0.40$ e/Å³). This reflects well the strong asymmetry of the O1–P bond lengths with $d(O1–P1) = 1.581(1)$ Å and $d(O1–P2) = 1.629(1)$ Å (Table 6). The corresponding deformation density peaks are less dissimilar in the DFT maps. The experimental and theoretical maps in the P1–O1–P2 plane (Figure 6) are also significantly different: peaks corresponding to the oxygen atom lone pairs are stronger in the DFT map whereas they are barely observable in the experimental maps. Another discrepancy is that the experimental map shows only charge accumulation along the internuclear axis, while theory displays both depletion and accumulation regions along this axis.

A dissimilarity in the bond lengths in the P1–O1–P2 moiety was also found in the structure of the NAD⁺, Li⁺ salt obtained

TABLE 5: Topological Characteristics of the Electron Density at the Covalent Bond Critical Points (CPs) of the Nicotinamide (a), the Adenine (b), and the Pyrophosphate (c) Moieties^a

(a) Nicotinamide										
bond	d_{1-2} (Å)	d_{2-cp} (Å)	d_{1-cp} (Å)	ρ_{cp} (e/Å ³)	$\nabla^2\rho$ (e/Å ⁵)	ϵ	λ_1 (e/Å ⁵)	λ_2 (e/Å ⁵)	λ_3 (e/Å ⁵)	
C21–O14	1.239(2)	0.486	0.486	0.754	–30.5	0.18	–27.8	–23.6	20.9	
C21–N7	1.336(2)	0.570	0.570	0.766	–21.4	0.23	–20.5	–16.7	15.8	
C20–N6	1.345(2)	0.533	0.533	0.815	–18.1	0.20	–18.1	–15.2	15.2	
C16–N6	1.349(1)	0.549	0.549	0.801	–20.2	0.17	–18.7	–16.0	14.6	
C17–C16	1.384(2)	0.645	0.645	0.741	–19.7	0.24	–16.7	–13.5	10.4	
C19–C20	1.386(2)	0.672	0.672	0.714	–20.9	0.24	–17.8	–14.3	11.2	
C17–C18	1.394(2)	0.654	0.654	0.742	–17.6	0.16	–15.5	–13.3	11.2	
C18–C19	1.397(2)	0.629	0.629	0.769	–18.3	0.15	–16.1	–14.0	11.1	
C15–N6	1.501(2)	0.611	0.611	0.891	–8.1	0.09	–11.5	–10.5	13.9	
HC18–C18	1.096	0.444	0.444	0.653	–20.9	0.11	–18.3	–16.5	13.9	
HC16–C16	1.092	0.376	0.376	0.718	–22.6	0.03	–19.5	–18.9	15.8	
HC17–C17	1.086	0.445	0.445	0.641	–21.2	0.13	–18.2	–16.0	12.9	
HC20–C20	1.082	0.387	0.387	0.695	–26.2	0.07	–20.7	–19.3	13.9	
HN7B–N7	1.036	0.266	0.266	0.770	–40.9	0.09	–33.7	–30.8	23.6	
HN7A–N7	1.037	0.268	0.268	0.770	–26.5	0.12	–28.7	–25.7	28.0	
ring						3.8	0.12	–0.2	1.9	2.1
(b) Adenine										
bond	d_{1-2} (Å)	d_{2-cp} (Å)	d_{1-cp} (Å)	ρ_{cp} (e/Å ³)	$\nabla^2\rho$ (e/Å ⁵)	ϵ	λ_1 (e/Å ⁵)	λ_2 (e/Å ⁵)	λ_3 (e/Å ⁵)	
C10–N4	1.323(2)	0.572	0.751	2.40	–18.3	0.14	–19.5	–17.1	18.3	
C10–N1	1.372(2)	0.594	0.785	2.12	–15.0	0.26	–17.9	–14.2	17.0	
C5–N1	1.465(2)	0.570	0.896	1.52	–8.8	0.14	–11.1	–9.8	12.1	
C9–N4	1.376(2)	0.615	0.763	2.10	–16.2	0.09	–16.8	–15.5	16.2	
C6–N1	1.366(2)	0.562	0.806	2.11	–17.5	0.26	–17.8	–14.1	14.4	
C9–C6	1.392(2)	0.669	0.726	2.12	–19.3	0.31	–17.2	–13.2	11.2	
C6–N2	1.353(2)	0.633	0.722	2.21	–14.2	0.19	–18.3	–15.4	19.5	
C9–C8	1.412(2)	0.683	0.73	2.02	–17.3	0.25	–16.0	–12.8	11.6	
C8–N5	1.319(2)	0.577	0.743	2.45	–23.2	0.23	–22.0	–17.9	16.7	
C8–N3	1.366(2)	0.567	0.802	2.08	–14.7	0.15	–16.6	–14.4	16.4	
C7–N2	1.314(2)	0.586	0.729	2.43	–22.9	0.12	–20.2	–18.0	15.3	
C7–N3	1.359(2)	0.575	0.786	2.22	–20.4	0.15	–18.1	–15.7	13.3	
HN3–N3	1.097	0.268	0.828	1.91	–34.5	0.01	–27.2	–27.0	19.7	
HN5A–N5	1.037	0.294	0.743	2.35	–45.3	0.05	–33.1	–31.6	19.4	
HN5B–N5	1.028	0.302	0.728	2.27	–37.1	0.08	–30.7	–28.4	22.0	
HC10–C10	1.089	0.439	0.655	1.85	–19.4	0.01	–16.9	–16.8	14.2	
HC7–C7	1.104	0.351	0.754	1.92	–23.4	0.03	–19.1	–18.5	14.2	
indole ring				0.33	8.5	0.1	–1.2	4.6	5.1	
imidazole ring				0.16	4.2	0.4	–0.4	1.8	2.8	
(c) Pyrophosphate										
bond	d_{1-2} (Å)	d_{1-cp} (Å)	d_{2-cp} (Å)	ρ_{cp} (e/Å ³)	$\nabla^2\rho$ (e/Å ⁵)	ϵ	λ_1 (e/Å ⁵)	λ_2 (e/Å ⁵)	λ_3 (e/Å ⁵)	
O1–P2	1.629(1)	0.661	0.968	1.27	3.7	0.20	–9.3	–7.8	20.9	
O1–P1(1)	1.581(1)	0.640	0.941	1.41	7.3	0.22	–11.3	–9.3	28.0	
P1–O2	1.498(1)	0.617	0.882	1.61	17.4	0.07	–11.6	–10.9	40.0	
P1–O3(1)	1.497(1)	0.614	0.884	1.63	20.7	0.29	–12.7	–9.8	43.2	
P2–O8	1.485(1)	0.617	0.871	1.58	22.6	0.05	–10.1	–9.7	42.4	
P2–O9	1.484(1)	0.607	0.877	1.77	20.0	0.07	–13.3	–12.4	45.7	
P1–O4	1.597(1)	0.648	0.949	1.30	5.7	0.14	–10.6	–9.3	25.7	
P2–O10	1.597(1)	0.653	0.945	1.27	8.1	0.17	–8.9	–7.6	24.6	
C1–O4	1.445(1)	0.576	0.872	1.49	–6.1	0.06	–11.2	–10.6	15.7	
C11–O10	1.442(2)	0.571	0.872	1.52	–5.3	0.15	–11.4	–9.9	16.0	

^a d_{1-2} is the bond length; d_{1-cp} and d_{2-cp} are the distances from the CP to the first and the second atoms defining the bond, respectively. ρ and $\nabla^2\rho$ denote the total electron density and its Laplacian at the critical point (CP). λ_1 , λ_2 , and λ_3 are the eigenvalues of the Hessian matrix of second derivatives $\{\partial^2\rho/\partial x_i\partial x_j\}$. ϵ is the ellipticity $\lambda_1/\lambda_2 - 1$.

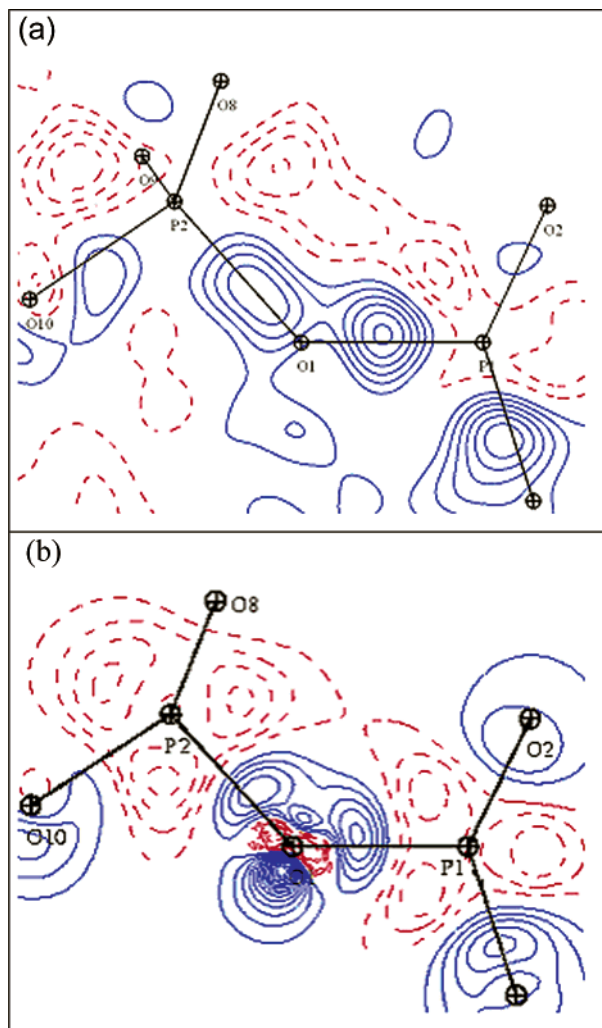


Figure 6. Static deformation electron density in the P1–O1–P2 phosphoester plane: (a) experimental; (b) theoretical. Contour $\pm 0.05 \text{ e}/\text{\AA}^3$.

from orthorhombic crystals: $d(\text{O1}–\text{P1}) = 1.56(1) \text{ \AA}$ and $d(\text{O1}–\text{P2}) = 1.66(1) \text{ \AA}$.⁴¹ In the complex of the aldose reductase protein with NADP⁺ and an inhibitor,⁹ we find a smaller and reversed (but possibly not statistically significant) discrepan-

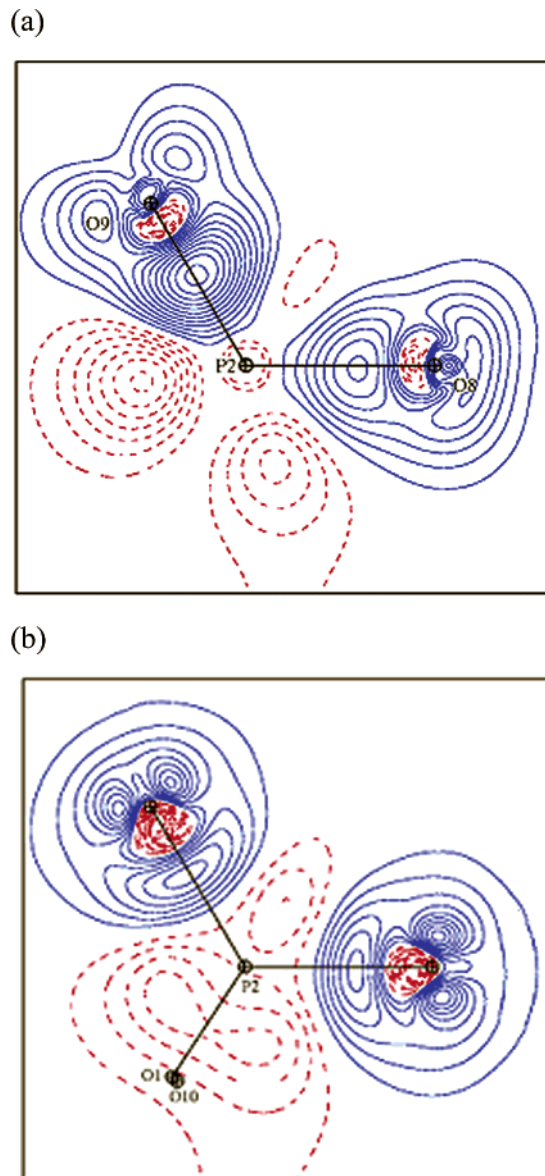


Figure 7. Static deformation electron density in the pyrophosphate O8–P2–O9 plane: (a) experimental; (b) theoretical. Contour $\pm 0.05 \text{ e}/\text{\AA}^3$.

TABLE 6: Geometrical and Topological Properties of the Electron Density at the D–H···A Hydrogen Bonds CPs^a

H-bond ^b	$d_{\text{D}\cdots\text{A}}$ (Å)	DHA (deg)	$d_{\text{H}\cdots\text{A}}$ (Å)	$d_{1-\text{cp}}$ (Å)	$d_{2-\text{cp}}$ (Å)	ρ_{cp} (e/Å ³)	$\nabla^2\rho$ (e/Å ⁵)	ϵ	λ_1 (e/Å ⁵)	λ_2 (e/Å ⁵)	λ_3 (e/Å ⁵)
O6–HO6···N4 ⁱⁱ	2.765	154.1	1.825	0.610	1.216	0.26	2.1	0.33	–1.8	–1.4	5.3
OW1–HW1B···N2 ^{ix}	2.980	176.8	2.010	0.734	1.284	0.12	2.1	0.05	–0.5	–0.5	3.2
N3–HN3···O2 ⁱⁱⁱ	2.618	174.4	1.516	0.481	1.044	0.51	0.5	0.10	–4.4	–4.0	9.1
N7–HN7B···O9 ^v	2.816	173.9	1.780	0.641	1.146	0.31	0.6	0.06	–2.2	–2.1	5.0
N5–HN5A···O3 ^{iv}	2.832	165.3	1.813	0.664	1.157	0.33	–0.1	0.01	–2.4	–2.3	4.5
N5–HN5B···O7 ^v	2.823	156.3	1.856	0.673	1.197	0.25	0.6	0.04	–1.8	–1.7	4.0
N7–HN7A···OW2 ^{viii}	2.972	173.1	1.937	0.684	1.261	0.12	2.2	0.87	–0.7	–0.4	3.4
O7–HO7···OW3 ⁱ	2.692	168.6	1.722	0.570	1.154	0.28	1.6	0.32	–2.2	–1.7	5.5
O12–HO12···O14 ^{vi}	2.722	156.5	1.786	0.605	1.189	0.21	2.4	0.39	–1.4	–1.0	4.9
OW4–HW4B···O13 ⁱⁱⁱ	2.778	175.9	1.800	0.715	1.112	0.36	3.6	0.08	–2.1	–2.0	7.8
O13–HO13···O6 ^{vii}	2.905	140.8	2.076	0.745	1.340	0.10	1.9	0.33	–0.4	–0.3	2.7
OW3–HW3B···O8 ⁱ	2.747	163.2	1.806	0.610	1.202	0.17	3.8	0.06	–0.8	–0.7	5.3
OW1–HW1A···O3 ⁱ	2.789	165.9	1.831	0.633	1.218	0.15	3.5	0.06	–0.7	–0.6	4.8
OW2–OW2A···OW1 ^x	2.810	175.4	1.838	0.623	1.230	0.14	3.5	0.10	–0.7	–0.6	4.9
OW2–HW2B···O6 ^{vi}	2.878	179.0	1.880	0.706	1.320	0.07	2.3	1.33	–0.6	–0.3	3.2
OW4–HW4A···O3 ⁱ	2.900	171.6	1.920	0.736	1.190	0.25	2.7	0.06	–1.3	–1.2	5.1
OW3–HW3A···OW2 ^j	2.946	169.6	1.984	0.690	1.318	0.08	2.4	0.36	–0.3	–0.2	3.0
C7–HC7···OW4 ^{vi}	3.082	163.1	2.013	0.755	1.263	0.14	1.6	0.64	–0.8	–0.5	2.9
C10–HC10···O4 ⁱ	3.253	133.3	2.025	0.955	1.467	0.05	0.7	0.49	–0.2	–0.2	1.1
C20–HC20···O9 ^v	3.035	155.6	2.148	0.744	1.279	0.13	1.4	0.47	–1.1	–0.7	3.2
C15–HC15···O8 ^v	3.231	165.7	2.400	0.844	1.306	0.12	1.2	0.13	–0.8	–0.7	2.7

^a ρ and $\nabla^2\rho$ denote the total electron density and the Laplacian at the CP. d_1 and d_2 are the distances from the CP to the first and the second atom defining the H-bond, respectively. ^b (i) X Y Z. (ii) X Y–1 Z. (iii) X Y+1 Z+1. (iv) X Y+1 Z+1. (v) X Y+1 Z. (vi) X Y Z+1. (vii) X–1 Y+1 Z. (viii) X Y+1 Z–1. (ix) X Y Z–1. (x) X–1 Y Z+1. (xi) X–1 Y Z. (xii) X+1 Y Z.

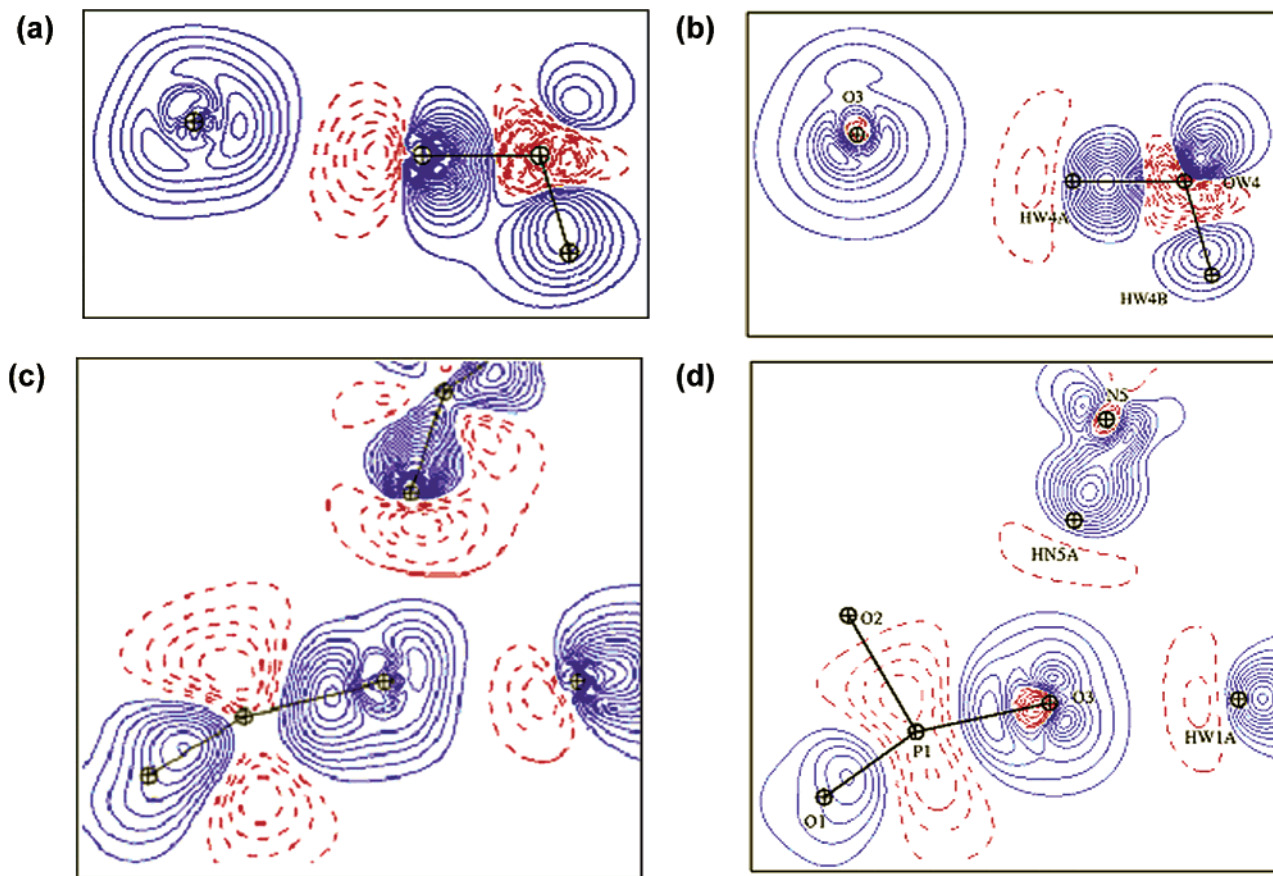


Figure 8. Static deformation electron density maps in the interaction planes P—O...H of hydrogen bonds involving the O3 pyrophosphate atom. Contour $\pm 0.05 \text{ e}/\text{\AA}^3$. In the O3...HW4A—OW4 plane: (a) experimental; (b) theoretical. In the HN5A^{x,y-1,z-1}—O3—HW1A plane: (c) experimental; (d) theoretical.

cy: $d(\text{O1—P1}) = 1.62(1) \text{ \AA}$ and $d(\text{O1—P2}) = 1.60(1) \text{ \AA}$. The variability of the O—P bond lengths may be attributed to strong crystal packing or intramolecular effects and to the different chemical environments on the neighboring lateral P=O and P—O[−] groups. P1—O3 and P1—O4 are hydrogen bond acceptors three times and one time, respectively. On the other hand, P2—O8 and P2—O9 receive both one hydrogen bond and one weak C—H...O interaction. Such apparent dissimilarity of O—P—O groups in NAD⁺ and NADP⁺ pyrophosphate structures was also observed for pentacovalent phosphorus in a trigonal bipyramidal R—O—PO₃—O—R' intermediate trapped in a phosphoryl transfer enzyme.⁴²

The four lateral P—O bonds have similar lengths and represent POO[−] groups where the negative charge is equally distributed on the two oxygen atoms. While all the lateral P—O groups display similar deformation density in the DFT maps, their experimental bonding density shows some variability (Figure 7). For instance, the P2—O8 and P2—O9 lateral bonds have equivalent lengths but the experimental deformation map shows nevertheless a discrepancy of $0.2 \text{ e}/\text{\AA}^3$ (Figure 7a).

The unshared electron pairs of the pyrophosphate lateral oxygen atoms are expected to be located in the POO[−] plane according to the sp² hybridization of the lateral PO₂ moiety. However, as shown on Figure 7a, the lone pairs peaks in the experimental deformation density do not lie in that plane, since, due to the hydrogen bond interactions, they are reoriented out of the POO[−] plane along the hydrogen bond path (Figure 8). Such behavior occurs for all lateral P—O bonds in the experimental maps.

The case of the O3 atom is noteworthy, as it participates in three hydrogen bonds: N5—HN5A...O3^{iv}, OW1—HW1A...O3ⁱ,

and OW4—HW4A...O3ⁱ (see Table 6 and Figures 8 and 9). In the experimental electron density maps, the stronger O3 lone pair peak is oriented toward the HW4A hydrogen atom (Figure 8a), whereas the other lone pair peak, shared between the two remaining hydrogen bonds, is weaker (Figure 8c). Therefore, in the experimental maps, the N5—HN5A...O3^{iv} and OW1—HW1A...O3ⁱ hydrogen bonds share the same O3 electron lone pair. These features are not reproduced in the theoretical deformation density map where the two electron lone pairs turn out to be oriented toward the HN5A and HW1A hydrogen atoms. The electron lone pair on the O3...HW4A path visible in the experimental map (Figure 8a) is not observed in the DFT map (Figure 8b).

The topological properties of the electron density (Table 5c), in particular the Laplacian and ρ_{cp} values, clearly differentiate the three pyrophosphate chemical bonds types: C—O(P), P—O(C), and P=O. The significant O1—P1 and O1—P2 bond lengths' discrepancy in the a priori symmetric P1—O1—P2 moiety is also reproduced by different Laplacian and electron density values at the CP. The O1—P2 bond is the longest among all O—P bonds and has the lowest charge density and Laplacian value.

Bond Lengths and Charge Density Topology. All chemical bonds of the NAD⁺ crystal are characterized by (3,−1) critical points. (3,+1) CPs are localized in the center of the pyrimidine and imidazole rings of the adenine base and of the nicotinamide pyridine ring (Figure 10). The topological properties of the nicotinamide and adenine moieties (Table 5a and b, Figure 11) also correlate well with the structural features, with a nice match between bond critical point (CP) densities, Laplacian values, and corresponding bond lengths (Table 6). The electron density

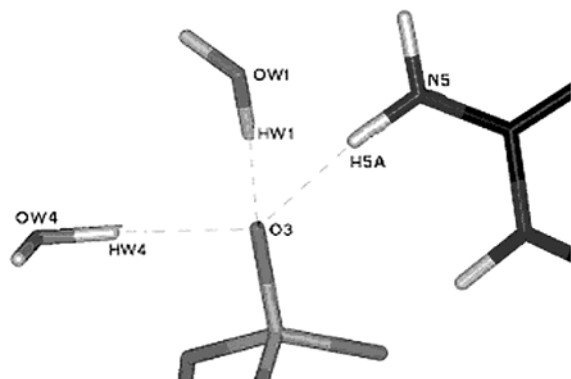


Figure 9. View of the triple hydrogen bonding pattern involving O3, HW4A, HW1A, and HN5A atoms.

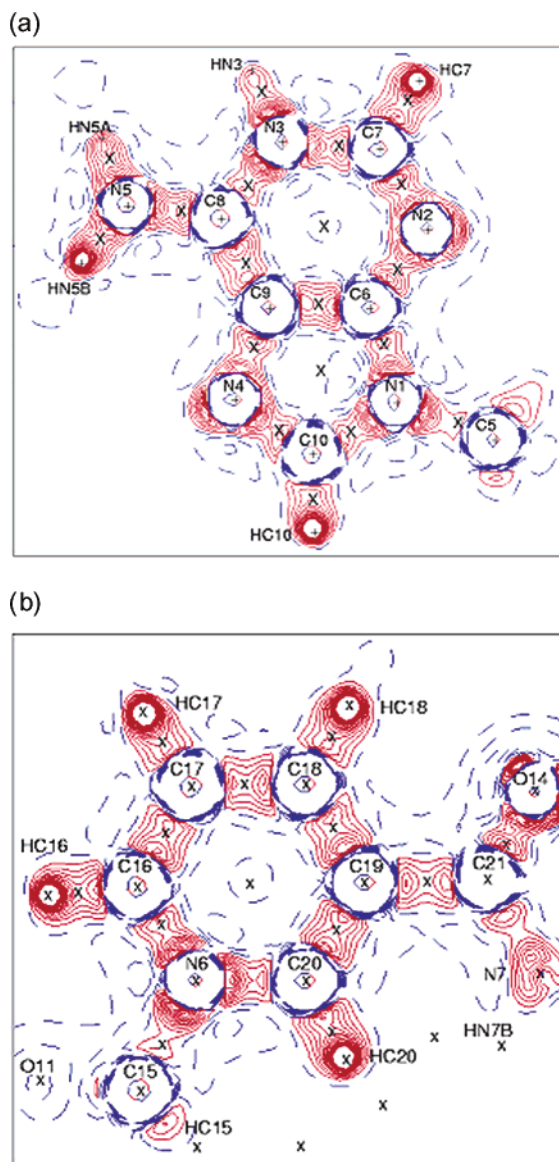


Figure 10. Laplacian of the total experimental electron density in the plane of the nicotinamide ring (a) and of the adenine ring (b). Contour $\pm 5e^{-}/\text{\AA}^5$. Positive in red; negative in blue. Atoms are noted with “+” symbols, and critical points are positions denoted with “x”.

at the CP clearly decreases smoothly as a function of the bond distance (Figure 11a), although a general relationship cannot be deduced, as these bonds involve different chemical species. However, the Laplacian and the total density at the CP allow a

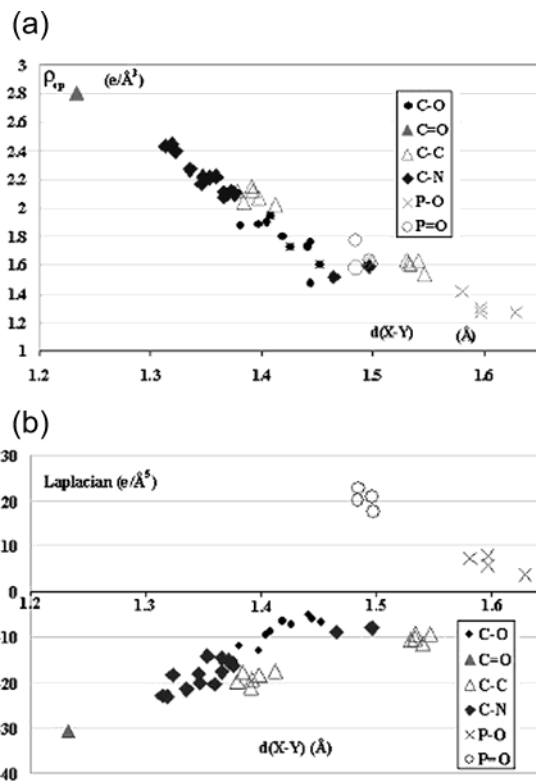


Figure 11. Electron density in $e/\text{\AA}^3$ (a) and Laplacian in $e/\text{\AA}^5$ (b) of the electron density at the bond critical point as a function of the interatomic distance (\AA).

classification of the various chemical bonds types, according to their interatomic distance, by gathering them per distinct bond type groups (Figure 11b). For instance, the Laplacian and charge density values at the bond critical points in the pyrophosphate group (Table 5c) allow a clear classification of the P–O bonds in two subtypes: $\nabla^2\rho = 6.2 \pm 1.9 e/\text{\AA}^5$ for single P–O bonds and $20.2 \pm 2.2 e/\text{\AA}^5$ for P=O double bonds.

Figure 11 also shows, as expected, that topological characteristics of C–C bond types depend on the hybridization of the carbon atoms. The $C(\text{sp}^2)\text{--}C(\text{sp}^2)$ bonds of the base rings and the ribose $C(\text{sp}^3)\text{--}C(\text{sp}^3)$ bonds are gathered in two distinct groups according to their Laplacian and charge density values. In the same way, the $C15\text{--}N6$ and $C5\text{--}N1$ bonds, which link the bases to the ribose groups, are longer than the other C–N bonds due to the sp^3 hybridization of the C15 and C5 carbon atoms. The values of their topological properties are also clearly distinct from those of the other C–N bonds.

Topology of Hydrogen Bonds. According to the theory of atoms in molecules,⁴³ a good criterion to decide if a polar nonbonded interaction of $\text{H}\cdots\text{acceptor}$ type can be defined as a hydrogen bond is the existence of a critical point along the $\text{H}\cdots\text{A}$ path. The geometrical and topological parameters of the 21 polar interactions $\text{H}\cdots\text{A}$ occurring in the NAD^+ crystal structure are reported in Table 6. All these interactions in the crystal, including weak $\text{C}\cdots\text{H}\cdots\text{O}$ interactions, are characterized by (3,–1) bond critical points.

From the results of a large number of charge density studies, Espinosa et al.²⁴ carried out an empirical analysis of the relationships between the geometry and the topological properties of the hydrogen bonds. These investigations allowed characterization of the $\text{X}\cdots\text{H}\cdots\text{O}$ hydrogen bonds by exponential relationships, relating topological properties to geometrical distances. In the NAD^+ crystal, the electron density at the CPs

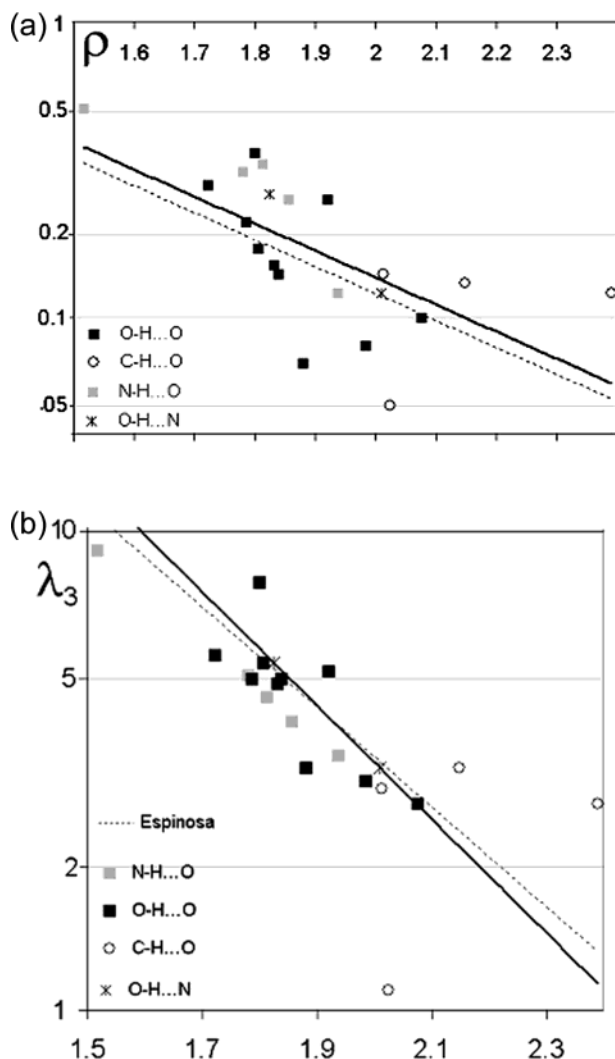


Figure 12. Topological properties at the hydrogen bonds' D-H...A critical points as a function of the H...A distance. The black curves are obtained by interpolation over the X-O...H interactions; the dashed curves are from the formula of Espinosa et al. (1999). (a) Total electron density ρ_{cp} . Fitted curve $\rho_{cp} = 9.2 \exp[-2.1d_{H\cdots A}]$. Equation from Espinosa: $\rho_{cp} = 8.0(4) \exp[-2.1(3)d_{H\cdots A}]$. (b) λ_3 curvature. Fitted exponential $\lambda_3 = 769 \exp[-2.7d_{H\cdots O}]$. Equation from Espinosa: $\lambda_3 = 410(80) \exp[-2.4(1)d_{H\cdots O}]$.

also varies according to an exponential relationship versus H...A distances:

$$\rho_{cp} = 8.0(4) \exp[-2.1(3)d(H\cdots A)]$$

This empirical relationship (Figure 12a), deduced from one experiment only (NAD⁺ crystal), is in good accordance with the equation given by Espinosa et al.,²⁴ within estimated standard deviations. The C-H...O interactions are located on the right part of the diagram, in the continuity of the other more polar hydrogen bonds. They are characterized by lower Laplacian and electron density values, in agreement with other geometrical features.

A high CP electron density associated with a negative Laplacian value denotes a covalent type interaction with shared electronic shells. The slightly negative Laplacian value of the N5-HN5A...O3=P1 hydrogen bond is probably not very meaningful with respect to the error on the Laplacian. This interaction is however the strongest among the three H-bonds involving atom O3, with a very short characteristic distance $d(H\cdots A) = 1.81$ Å and a strong density at the critical point (ρ_{cp}

$= 0.33 \text{ e/Å}^3$). There are some other N-H...O=P hydrogen bonds which are even shorter with large electron density at the CP, but they show positive Laplacian values (Table 6).

In the present study, the evolution of the λ_3 eigenvalues also follows an exponential law similar to that calculated by Espinosa et al.²⁴ (Figure 12b) but with some outliers such as N3-H3...O2, which is the strongest hydrogen bond, in terms of geometrical characteristics, in the whole structure.

Atomic Charges. The net charges for different chemical groups calculated after the multipolar refinement ($q = P_v - N_v$) are compared to Mulliken charges in Table 7. Both the experimental and theoretical charges of the NAD⁺ groups display an accumulation of positive charges on the bases and of negative charges in the pyrophosphate regions. This is related to the N3-protonation of the adenine base and to the coordination of the nicotinamide nitrogen atoms N6.

The two ribose rings on the nicotinamide and adenine sides have the same chemical formula, but their global experimental charges are dissimilar: nearly $-0.9(3)$ and $0.0(3)$ e, respectively (Table 7). These numbers must be analyzed with their standard deviations even if the nonequivalence of the two ribose rings charges is related to the asymmetry of the central O1-P1-O2 moiety. Furthermore, the adenine-side ribose is involved in five hydrogen bonds, two times as donor and three times as acceptor, while the nicotinamide-side ribose accepts one and donates one hydrogen bond (Table 6). The discrepancy of the experimental charges between the two ribose groups is not reproduced by the Mulliken population analysis (MPA) of SIESTA calculations (Table 7). The MPA charges show a charge transfer between periodic and "gas phase" calculations, from the pyrophosphate group ($+0.16$ e), the water molecule 1 ($+0.07$ e), and the adenine-side ribose ($+0.04$ e) to the adenine base (-0.16 e), the nicotinamide base (-0.11 e), and the nicotinamide-side ribose (-0.04 e). This is consistent with the hydrogen bonding network in the crystal packing. Gas phase calculations on the same crystallographic coordinates using Gaussian 98³⁶ with MP2, Hartree-Fock, and B3LYP functionals have shown a similar equivalence between the two ribose groups: MP2, 0.35 and 0.33 e; B3LYP, 0.22 and 0.24 e; on the adenine and nicotinamide sides, respectively. This is in accordance with the results obtained from the SIESTA "gas phase" calculation. SIESTA results are very close to B3LYP ones, and the major difference between ab initio and DFT methods is the pyrophosphate group total charge.

Electrostatic Potential. The electrostatic potential generated by NAD⁺ isolated from the crystal lattice was computed from the experimental and theoretical electron density distributions. The positive and negative potential areas around the nicotinamide ring display generally a good similarity. The positions of negative potential peaks in the pyrophosphate region are in good agreement in the two studies.

Although the general shapes (zero contour surface and spatial extension) of the potentials are very close, there are some quantitative discrepancies within the closer neighborhood of the atoms. Around the amide oxygen atom O14, the experimental electronegative potential is two times weaker than the theoretical one (Figure 13). This is in agreement with the relative peak heights of the two electron lone pairs of the oxygen atom, which are reversed (Figure 3a and b).

Also the negative well of electrostatic potential around the pyrophosphate group, in the vicinity of P1-O1, is -0.30 and -0.50 e/Å in the experimental and theoretical maps, respectively (Figure 13). The negative potential extends further in the ether oxygen region in the experimental map. For the adenine group

TABLE 7: Net Charges (e) of the Different Groups Constituting the NAD⁺ Molecule^a

group	exp	total charge				
		Siesta periodic (triclinic)	Siesta "gas phase"	Gaussian 98 gas phase MP2	Gaussian 98 gas phase HF	Gaussian 98 gas phase B3LYP
pyrophosphate	−2.1 (3)	−1.96	−2.01	−2.43	−2.44	−2.09
>CH ₂ (C1)	0.5 (1)	0.35	0.34	0.38	0.40	0.31
>CH ₂ (C11)	0.4 (1)	0.35	0.34	0.38	0.39	0.30
ribose aden.	0.0 (3)	0.26	0.27	0.35	0.35	0.22
ribose nicot.	−0.9 (3)	0.29	0.28	0.33	0.32	0.24
adenine base	1.4 (3)	0.38	0.47	0.52	0.51	0.56
nicotine base	0.7 (3)	0.40	0.40	0.46	0.45	0.54
amide	−0.0 (2)	0.00	0.05	0.09	0.09	0.03
4H ₂ O	−0.0	−0.07	−0.14	−0.08	−0.12	−0.11

^a The uncertainty is given between parentheses. The periodic triclinic theoretical calculation is reported. For comparison nonperiodic (gas phase) calculations with Siesta and Gaussian98 are also reported.

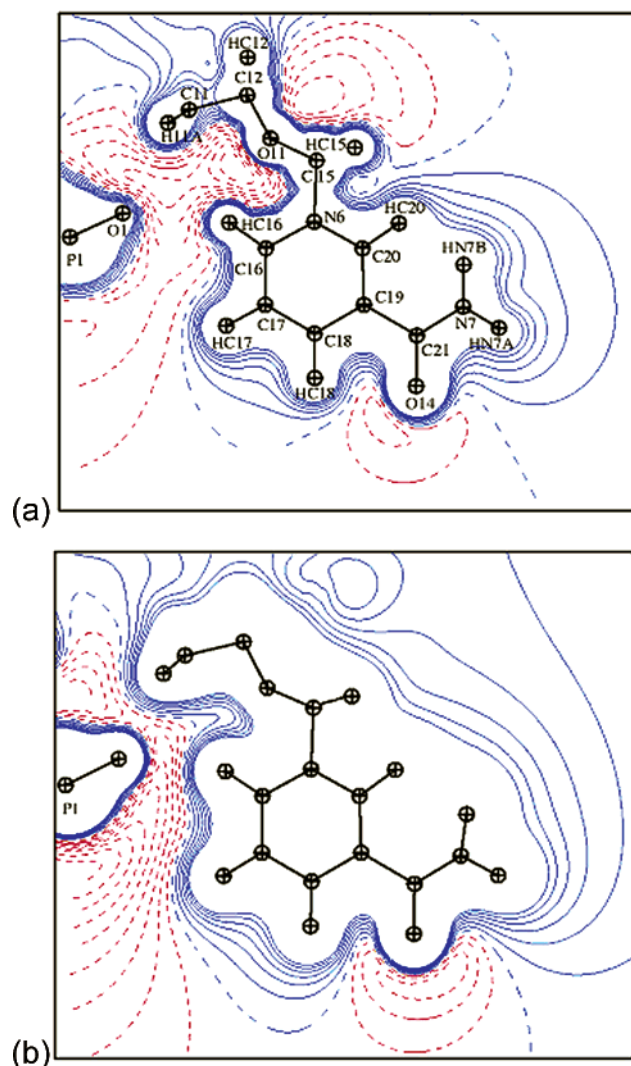


Figure 13. Electrostatic potential around the nicotinamide plane generated by a NAD⁺ molecule isolated from the crystal: (a) experimental; (b) theoretical. Contours ± 0.05 e/Å. Positive in blue; negative in red; zero in blue dashed line.

(figure not shown), the spatial extensions are similar; the only significant discrepancy is located in the vicinity of the N4 atom, due to a stronger nitrogen electron lone pair in the theoretical deformation map compared to the experiment (Figure 4).

The electrostatic potential generated by a molecule is a major driving force in the intermolecular interactions. NAD⁺ is usually found as a coenzyme in proteins, and its positioning is directly related to the electrostatic potential complementarity between

the ligand and the active site of the enzyme. This feature is clearly observed in the electrostatic potential maps of the aldose reductase complex, for which negative and positive potential regions around the cofactor correspond to areas of the enzyme active site of opposite sign.⁴⁴ These results strongly suggest that electrostatic interactions are likely to be the dominant factor in the binding of the NAD⁺ cofactor with enzymes. These interactions between the protein and the cofactor extend beyond the typical H-bond range. As shown in Figure 13, the electrostatic potential spatial extension from the atomic nuclei to the zero potential line value goes up to 4–7 Å for negative values and 3–5 Å for positive values.

Conclusions

This crystallographic investigation has provided detailed information about the electron distribution of NAD⁺. A quantitative characterization of the covalent bonds and of the hydrogen bonds has been obtained through the topological analysis of the total electron density. Besides a better understanding of the redox processes involving NAD⁺, the present crystallographic analysis was also performed to complete the database of multipolar parameters¹¹ describing the electron density of polypeptides and nucleic acids.

The deformation electron densities obtained at the end of the multipolar refinement were compared with those calculated by DFT with the software SIESTA²⁶ for the calibration of the application to biological molecules, notably nucleic acids. These comparisons allow us thus to determine the minimal bases to be used with the program SIESTA in order to obtain reliable theoretical electron densities compared to the experimental results. This principle of comparison being validated, the selected bases will be employed thereafter in theoretical calculations on protein and nucleic acid structures known at atomic resolution.

Acknowledgment. N.M. was supported by a grant of the Association pour la Recherche sur le Cancer, and B.G., by a fellowship of the French Minister of Research and Technology. The authors thank Dr. Marivi Fernandez-Serra and Pr. Bernard Vitoux for very useful discussions.

Supporting Information Available: CIF file of NAD⁺ and charge density parameters (Table S1). The values of the rigid bond test $|\Delta Z| = |Z_A - Z_B|$, where Z_A and Z_B are the projections of the thermal displacement parameters along the covalent bond (A–B) directions are given in Table S2. The residual electron density maps in the nicotinamide and adenine plane are given in Figure S1. The structure will be deposited at the Nucleic Acids Database. This material is available free of charge via the Internet at <http://pubs.acs.org>.

References and Notes

- (1) Carugo, O.; Argos, P. *Proteins: Struct., Funct., Genet.* **1997**, *28*, 10.
- (2) Carugo, O.; Argos, P. *Proteins: Struct., Funct., Genet.* **1997**, *28*, 29.
- (3) Wu, Y. D.; Houk, K. N. *J. Am. Chem. Soc.* **1991**, *113*, 2353.
- (4) Donkersloot, M. C. A.; Buck, H. M. *J. Am. Chem. Soc.* **1981**, *103*, 6554.
- (5) Meijers, R.; Morris, R. J.; Adolph, H. W.; Merlii, A.; Lamzin, V. S.; Cedergren-Zeppeauer, E. S. *J. Biol. Chem.* **2001**, *276*, 9316.
- (6) Miwa, Y.; Mizuno, T.; Tsuchida, K.; Taga, T.; Iwata, Y. *Acta Crystallogr.* **1999**, *B55*, 78.
- (7) Pavelites, J. J.; Gao, J.; Bash, P. A.; Mackerell, A. D. *J. Comput. Chem.* **1997**, *18*, 221.
- (8) Espinosa, E.; Lecomte, C.; Molins, E.; Veintemillas, S.; Cousson, A.; Paulus, W. *Acta Crystallogr.* **1996**, *B52*, 519.
- (9) Guillot, B.; Muzet, N.; Jelsch, C.; Lecomte, C.; Mitschler, A.; Chevrier, B.; Howard, E.; Podjarny, A. 20th European Crystallography Meeting, Krakow, 2001, Aug 25–31.
- (10) Guillot, B.; Lecomte, C.; Cousson, A.; Scherf, C.; Jelsch, C. *Acta Crystallogr.* **2001**, *D57*, 981–989.
- (11) Pichon-Pesme, V.; Lecomte, C.; Lachezar, H. *J. Phys. Chem.* **1995**, *99*, 6242.
- (12) Guillot, B.; Jelsch, C.; Lecomte, C. *Acta Crystallogr.* **2000**, *C56*, 726.
- (13) *COLLECT: Data Collection Software*; Nonius BV: Delf, The Netherlands, 1998.
- (14) Otwinowski, Z.; Minor, W. *Methods Enzymol.* **1997**, *276*, 307.
- (15) Guillot, B.; Viry, L.; Guillot, R.; Lecomte, C.; Jelsch, C. *J. Appl. Crystallogr.* **2001**, *34*, 214.
- (16) Lenstra, A. T. H.; Van Loock, J. F. J.; Rousseau, B.; Maes, S. T. *Acta Crystallogr.* **2000**, *A56*, 300.
- (17) Hansen, N. K.; Coppens, P. *Acta Crystallogr.* **1978**, *A34*, 909.
- (18) Stewart, R. F.; Davidson, E. R.; Simpson, W. T. *J. Chem. Phys.* **1965**, *43*, 175.
- (19) Clementi, E.; Raimondi, D. L. *J. Chem. Phys.* **1963**, *41*, 2686.
- (20) Cromer, D. T. *International Tables for X-ray Crystallography*; Kynoch Press: Birmingham, 1974.
- (21) Pichon-Pesme, V.; Lecomte, C.; Wiest, R.; Benard, M. *J. Am. Chem. Soc.* **1992**, *114*, 2713.
- (22) Hirshfeld, F. L. *Acta Crystallogr.* **1976**, *A32*, 239.
- (23) Bouhmaida, N.; Ghermani, N. E.; Lecomte, C.; Thalal, A. *Acta Crystallogr.* **1999**, *A55*, 729.
- (24) Espinosa, E.; Souhassou, M.; Lachezar, H.; Lecomte, C. *Acta Crystallogr.* **1999**, *B55*, 563.
- (25) Souhassou, M.; Blessing, R. H. *J. Appl. Crystallogr.* **1999**, *32*, 210.
- (26) Sanchez-Portal, D.; Ordejon, P.; Artacho, E.; Soler, J. M. *Int. J. Quantum Chem.* **1997**, *65*, 453.
- (27) Soler, J. M.; Artacho, E.; Gale, J. D.; Garcia, A.; Junquera, J.; Ordejon, P.; Sanchez-Portal, D. *J. Phys.: Condens. Matter* **2002**, *14*, 2745.
- (28) Artacho, E.; Sanchez-Portal, D.; Ordejon, P.; Garcia, E.; Soler, J. M. *Phys. Status Solidi B* **1999**, *215*, 809.
- (29) Kohn, W.; Sham, L. J. *Phys. Rev.* **1965**, *140*, 1133.
- (30) Perdew, J. P.; Burke, K.; Ernzerhof, M. *Phys. Rev. Lett.* **1996**, *77*, 3865.
- (31) Troullier, N.; Martins, J.-L. *Phys. Rev. B* **1991**, *43*, 1993.
- (32) Kleinman, L.; Bylander, D. M. *Phys. Rev. Lett.* **1982**, *48*, 1425.
- (33) Sankey, O. F.; Niklewski, D. J. *Phys. Rev. B* **1989**, *40*, 3979.
- (34) Domene, C.; Fowler, P. W.; Jemmer, P.; Madden, P. *Chem. Phys. Lett.* **1999**, *299*, 51.
- (35) Greatbanks, S. P.; Gready, J. E.; Limaye, A. C.; Rendell, A. P. *J. Comput. Chem.* **2000**, *21* (9), 788.
- (36) Frisch, M. J.; Trucks, G. W.; Schlegel, H. B.; Scuseria, G. E.; Robb, M. A.; Cheeseman, J. R.; Zakrzewski, V. G.; Montgomery, J. A., Jr.; Stratmann, R. E.; Burant, J. C.; Dapprich, S.; Millam, J. M.; Daniels, A. D.; Kudin, K. N.; Strain, M. C.; Farkas, O.; Tomasi, J.; Barone, V.; Cossi, M.; Cammi, R.; Mennucci, B.; Pomelli, C.; Adamo, C.; Clifford, S.; Ochterski, J.; Petersson, G. A.; Ayala, P. Y.; Cui, Q.; Morokuma, K.; Salvador, P.; Dannenberg, J. J.; Malick, D. K.; Rabuck, A. D.; Raghavachari, K.; Foresman, J. B.; Cioslowski, J.; Ortiz, J. V.; Baboul, A. G.; Stefanov, B. B.; Liu, G.; Liashenko, A.; Piskorz, P.; Komaromi, I.; Gomperts, R.; Martin, R. L.; Fox, D. J.; Keith, T.; Al-Laham, M. A.; Peng, C. Y.; Nanayakkara, A.; Challacombe, M.; Gill, P. M. W.; Johnson, B.; Chen, W.; Wong, M. W.; Andres, J. L.; Gonzalez, C.; Head-Gordon, M.; Replogle, E. S.; Pople, J. A. *Gaussian, Inc.*: Pittsburgh, PA, 2001.
- (37) Fernandez-Serra, M. V.; Junquera, J.; Jelsch, C.; Lecomte, C.; Artacho, E. *Solid State Commun.* **2000**, *116*, 395.
- (38) Taylor, R.; Kennard, O. *J. Mol. Struct.* **1982**, *78*, 1.
- (39) Cunane, L. M.; Taylor, M. R. *Acta Crystallogr.* **1997**, *D53*, 765.
- (40) Cunane, L. M.; Taylor, M. R. *Acta Crystallogr.* **1993**, *B49*, 524.
- (41) Reddy, B. S.; Saenger, W.; Mühlegger, K.; Weimann, G. *J. Am. Chem. Soc.* **1981**, *103*, 907.
- (42) Lahiri, S. D.; Zhang, G.; Dunaway-Mariano, D.; Allen, K. N. *Science* **2003**, *299*, 2067.
- (43) Bader, R. W. F. *Atoms in Molecules. A Quantum Theory*; Oxford Science Publications: Oxford, 1990.
- (44) Muzet, N.; Guillot, B.; Jelsch, C.; Lecomte, C. *Proc. Natl. Acad. Sci. U.S.A.*, in press.
- (45) Burnett, M. N.; Johnson, C. K. *ORTEP—III: Oak Ridge Thermal Ellipsoid Plot Program for Crystal Structure Illustrations*; Oak Ridge National Laboratory Report ORNL-6895; 1996.